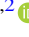
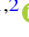

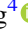









Parker Solar Probe Observations of Alfvénic Waves and Ion-cyclotron Waves in a Small-scale Flux Rope

Chen Shi^{1,2} , Jinsong Zhao^{1,2} , Jia Huang³ , Tiejian Wang⁴ , Dejin Wu¹ , Yu Chen⁵ , Qiang Hu^{5,6} ,
Justin C. Kasper^{3,7} , and Stuart D. Bale^{8,9,10,11} 

¹ Key Laboratory of Planetary Sciences, Purple Mountain Observatory, Chinese Academy of Sciences, Nanjing 210023, People's Republic of China
js_zhao@pmo.ac.cn

² School of Astronomy and Space Science, University of Science and Technology of China, Hefei 230026, People's Republic of China

³ Climate and Space Sciences and Engineering, University of Michigan, Ann Arbor, MI 48109, USA

⁴ RAL Space, STFC, Oxfordshire OX11 0QX, UK

⁵ Department of Space Science, The University of Alabama in Huntsville, Huntsville, AL 35805, USA

⁶ Center for Space Plasma and Aeronomic Research (CSPAR), The University of Alabama in Huntsville, Huntsville, AL 35805, USA

⁷ Smithsonian Astrophysical Observatory, Cambridge, MA 02138, USA

⁸ Space Sciences Laboratory, University of California, Berkeley, CA 94720-7450, USA

⁹ Physics Department, University of California, Berkeley, CA 94720-7300, USA

¹⁰ The Blackett Laboratory, Imperial College London, London, SW7 2AZ, UK

¹¹ School of Physics and Astronomy, Queen Mary University of London, London E1 4NS, UK

Received 2020 December 10; revised 2021 January 15; accepted 2021 January 16; published 2021 February 15

Abstract

Small-scale flux ropes (SFRs) are common in the interplanetary environment. However, previous identification procedures generally discard SFRs with medium and high Alfvénicity, which are thought to be Alfvénic waves or Alfvénic structures. This paper first identifies an SFR event with medium Alfvénicity in the inner heliosphere (at ~ 0.2 au) using Parker Solar Probe measurements. We find Alfvénic waves that arise inside SFR based on high correlations between the magnetic field and velocity fluctuations. We also observe quasi-monochromatic electromagnetic waves with frequencies f that are usually larger than the local proton cyclotron frequency at the leading and trailing edges of this SFR. These waves are well explained by the outward-propagating ion-cyclotron waves, which have wave frequencies ~ 0.03 – 0.3 Hz and wavelengths ~ 60 – 2000 km in the plasma frame. Moreover, we show that the power spectral density of the magnetic field in SFR middle region follows the power-law distribution, where the spectral index changes from -1.5 ($f \lesssim 1$ Hz) to -3.3 ($f \gtrsim 1$ Hz). These findings would motivate developing an automated program to identify SFRs with medium and high Alfvénicity from Alfvénic waves/structures.

Unified Astronomy Thesaurus concepts: Solar wind (1534); Space plasmas (1544); Plasma physics (2089)

1. Introduction

Magnetic flux ropes, which possess helical magnetic field topology, play important roles in transferring the mass, momentum, and energy in the interplanetary environment and in affecting space weather (e.g., Liu et al. 2014; Shen et al. 2014, 2017; Huang et al. 2017, 2018; Kilpua et al. 2017). Interplanetary magnetic flux ropes are usually classified into two categories: small-scale magnetic flux ropes (SFRs; e.g., Moldwin et al. 1995, 2000; Hu et al. 2018), and magnetic clouds (large-scale magnetic flux ropes; e.g., Klein & Burlaga 1982). Generally, SFRs have durations from a few minutes to a few hours, which is much shorter than the duration of magnetic clouds ~ 20 hr (e.g., Feng et al. 2008; Cartwright & Moldwin 2010). Contrary to magnetic clouds that are widely thought of as originating from the Sun (e.g., Klein & Burlaga 1982), the source of SFRs is still controversial: the Sun and/or the interplanetary space (e.g., Feng et al. 2007, 2008; Cartwright & Moldwin 2008, 2010; Zank et al. 2017; Hu et al. 2018; Zheng & Hu 2018). To study the source and the distribution of SFRs, statistical analyses have been performed for SFRs at heliocentric distances from 0.29 to 7–8 au through observations from Helios, Wind, Advanced Composition Explorer, Ulysses, and Solar TErrestrial RELations Observatory (Moldwin et al. 1995, 2000; Feng et al. 2007, 2008; Cartwright & Moldwin 2008, 2010; Tian et al. 2010; Yu et al. 2014, 2016; Hu et al. 2018; Zheng & Hu 2018; Chen et al. 2019; Chen & Hu 2020). Recently, using the Parker Solar Probe (PSP), Zhao et al. (2020a, 2020b) and

Chen et al. (2020) explored the distribution of SFRs at the heliocentric distance down to ~ 0.13 au.

Similar to SFRs, Alfvénic structures in the solar wind also exhibit helical magnetic field configuration (e.g., Zhao et al. 2020a, 2020b). To exclude these Alfvénic structures, different criteria are employed in different automated identification programs of SFRs. For example, Chen et al. (2020) use a criterion, i.e., the Walén slope smaller than 0.3, to distinguish SFRs from Alfvénic structures and fluctuations in the Grad–Shafranov-based program. Zhao et al. (2020a, 2020b) identify SFRs with parameters including normalized magnetic helicity $|\sigma_m| \geq 0.7$, normalized cross helicity $|\sigma_c| \leq 0.3$, and normalized residual energy $\sigma_r \leq -0.5$ through an automated program based on the wavelet analysis (Telloni et al. 2013). In fact, Alfvénic waves can embed within an SFR. Gosling et al. (2010) identified such an event (the duration ~ 3 hr) in which the Walén slope is ~ 0.62 . Since SFRs with medium and high Alfvénicity were removed in previous identification programs (e.g., Cartwright & Moldwin 2008, 2010; Yu et al. 2014, 2016; Hu et al. 2018; Zheng & Hu 2018; Chen et al. 2019, 2020; Chen & Hu 2020; Zhao et al. 2020a, 2020b), we have little knowledge of these kinds of SFRs.

Using PSP measurements, this paper gives direct observational evidence for the SFR with medium Alfvénicity in the inner heliosphere. Also, we find this SFR contains both large-scale Alfvénic waves and small-scale electromagnetic waves, and the latter waves are identified as the ion-cyclotron mode wave based

on the wave theory in the spacecraft frame. This paper uses the data detected by the Electromagnetic Fields Investigation (FIELDS; Bale et al. 2016) and Solar Wind Electrons Alphas and Protons (SWEAP; Kasper et al. 2016) instruments on PSP (Fox et al. 2016), which provide vector magnetic fields with temporal resolution 0.0137 s and the plasma parameters with temporal resolution 0.874 s during the time interval including our SFR event.

2. Event Overview

Our SFR event arises during the time interval of 08:34:45 UT–08:46:05 UT on 2018 November 1, and its duration is about ~ 11 minutes. We identify the SFR edges arising at 08:34:45 UT and 08:46:05 UT through the obvious changes of the magnetic field direction (Figure 1(a)) and of the solar wind bulk flow V_{\parallel} along the magnetic field (Figure 1(f)) therein. Figure 1(a) also shows that this event is embedded in a highly variable magnetic field environment. Different from varying magnetic field, the solar wind is steadily flowing outward from the Sun at a speed of ~ 325 km s $^{-1}$, which corresponds to the slow solar wind condition, as shown in Figure 1(b). Moreover, Figures 1(c)–(e) zoom in the magnetic field and the velocity during 08:25:00 UT–08:55:00 UT, and here the magnetic field data are averaged down to the plasma measurement cadence 0.874 s. Figures 1(c)–(e) show positive correlations between magnetic field and velocity perturbations. Figure 1(f) presents the distributions of V_{\parallel} and the Alfvén speed $V_A = B/(\mu_0 n_p m_p)^{1/2}$, where n_p is the proton number density. Inside SFR, V_{\parallel} approximates 300 km s $^{-1}$, which is much larger than $V_A \simeq 60$ km s $^{-1}$. V_{\parallel} becomes smaller than V_A nearby the SFR edges. Large V_{\parallel} could result in a significant Doppler frequency shift of the waves in our event. The plasma parameters, e.g., proton number density n_p (Figure 1(g)), proton temperature T_p (Figure 1(h)), and proton beta β_p (Figure 1(i)), are nearly stable both inside and outside of this SFR, where $n_p \simeq 220$ cm $^{-3}$, $T_p \simeq 12$ eV, and $\beta_p \simeq 1$. Furthermore, Figure 1(j) presents the pitch angle distribution of electrons at the energy of 315 eV. The $E_e = 315$ eV electrons observed by PSP are proposed to be proxy of strahl electrons in the solar wind (Nieves-Chinchilla et al. 2020). Figure 1(j) shows that bidirectional electrons with $E_e = 315$ eV arising at $\theta = 0^\circ$ and $\theta = 180^\circ$ inside SFR. The enhanced bidirectional strahl electrons are considered robust signatures for the flux rope in the solar wind (Nieves-Chinchilla et al. 2020). We also see antiparallel and bidirectional $E_e = 315$ eV electrons arising in upstream and downstream regions, respectively, indicating that this SFR resides between open and closed magnetic field structures.

Figures 1(k)–(m) present normalized magnetic helicity $\sigma_m(s, t) = 2 \text{Im}(B_T^*(s, t)B_N(s, t))/|B(s, t)|^2$, normalized cross helicity $\sigma_c(s, t) = 2\langle V(s, t) \cdot V_B(s, t) \rangle / (\langle V(s, t)^2 \rangle + \langle V_B(s, t)^2 \rangle)$, and normalized residual energy $\sigma_r(s, t) = (\langle V(s, t)^2 \rangle - \langle V_B(s, t)^2 \rangle) / (\langle V(s, t)^2 \rangle + \langle V_B(s, t)^2 \rangle)$ distributions using the wavelet transform method (Grinsted et al. 2004), where s is the wavelet scale, and $V_B = B/(\mu_0 n_p m_p)^{1/2}$ denotes the magnetic field in the Alfvén speed unit. Figures 1(k)–(m) show that $\sigma_m \sim -0.20$, $\sigma_c \sim 0.55$, and $\sigma_r \sim -0.79$ at the scale of ~ 11 minutes. Moreover, we find σ_c within SFR can reach 0.69 in the scale of ~ 0.1 –1 minute, which implies the existence of Alfvénic waves (also see Figure 2). Alfvénic waves with the scale of ~ 0.1 –1 minute also exist in SFR surrounding regions where σ_c can reach 0.88.

To further show the structure of our identified SFR, Figures 1(n) and (o) give the results by using the Grad–Shafranov reconstruction technique (Hau & Sonnerup 1999;

Hu & Sonnerup 2001, 2002). The Grad–Shafranov reconstruction map (Figure 1(n)) clearly shows the existence of the flux rope structure, and its scale size is about 0.0009 au. Moreover, the Grad–Shafranov reconstruction indicates the duration of this SFR, i.e., from 08:34:23 UT to 08:43:15 UT, which is largely consistent with the result based on the change of the magnetic field and plasma parameter distributions (see Figures 1(c)–(j)). This indicates that although the Grad–Shafranov reconstruction technique uses the ideal MHD equation and the rigid body assumption for the flux rope, it can reconstruct the SFR with modest Alfvénicity over the time interval 08:34:23 UT–08:43:15 UT for which the Walén test slope is about 0.32 (Chen et al. 2020).

3. Wave Analysis

Figure 2 presents the wave analysis for low-frequency electromagnetic fluctuations during 08:25:00 UT–08:55:00 UT. Figures 2(b)–(e) exhibit the wavelet cross-coherence spectra of $B_{\perp} - V_{\perp}$ through the wavelet coherence analysis (Grinsted et al. 2004). To obtain the correlation of $B_{\perp} - V_{\perp}$ between 0.02 and 0.57 Hz, we first smooth B at a timescale of 60 s, which is considered as the background magnetic field B_0 , and then transform B and V_p into $(B_{\perp}, B_{\parallel})$ and $(V_{\perp}, V_{\parallel})$ in the field-aligned coordinates. Figures 2(b) and (d) show that the coherence coefficient $CC(B_{\perp}, V_{\perp})$ can be larger than 0.6 for low-frequency fluctuations with $f \sim 0.02$ –0.3 Hz inside and outside of the SFR, indicating the existence of low-frequency Alfvénic waves. Figures 2(c) and (e) show that the coherence phase angle $\Psi(B_{\perp}, V_{\perp})$ is mainly around zero in regions with high $CC(B_{\perp}, V_{\perp})$, which corresponds to Alfvénic waves propagating against the magnetic field.

Figures 2(f)–(i) further give the distributions of degree of polarization (DOP), wave normal angle θ_k , ellipticity (ϵ), and power spectral density of B (B_{PSD}) using the singular value decomposition method (e.g., Santolík et al. 2003). To clearly show quasi-monochromatic waves, we retain the data with $\text{DOP} \gtrsim 0.7$, $\epsilon \lesssim -0.65$ and $\theta_k \lesssim 25^\circ$ in Figures 2(f)–(h). It is interesting to see that quasi-monochromatic waves with frequencies $f \simeq 0.3$ –4 Hz arise near the leading and trailing edges of this SFR, where the proton cyclotron frequency f_{cp} is about 0.3 Hz. These waves have small angles ($\theta_k \lesssim 25^\circ$) and exhibit left-hand polarization ($\epsilon < -0.65$). Moreover, the observed quasi-monochromatic waves locate in the turbulent medium, as suggested by Figure 2(i). Figures 2(j) and (k) further compare B_{PSD} in different regions, e.g., the upstream region during 08:30:00 UT–08:34:00 UT, the leading region during 08:35:00 UT–08:38:00 UT, the middle region during 08:39:00 UT–08:43:00 UT, the trailing region during 08:44:00 UT–08:46:00 UT, and the downstream region during 08:47:00 UT–08:51:00 UT. Figure 2(j) shows that B_{PSD} in the range of ~ 0.3 –4 Hz enhances in both SFR leading and trailing regions, and B_{PSD} in the SFR middle region follows a power-law distribution, i.e., $B_{\text{PSD}} \propto f^{-1.5}$ at $f \lesssim 1$ Hz and $B_{\text{PSD}} \propto f^{-3.3}$ at $f \gtrsim 1$ Hz. In Figure 2(k), both upstream and downstream B_{PSD} obey the power-law distribution similar to that in the SFR middle region. This implies the same turbulence cascade mechanism inside and outside of the SFR. Since the Doppler shift frequencies of the proton inertial length and the proton gyroradius are about 3.2 and 3 Hz, the observed B_{PSD} in the SFR middle region extends to sub-ion scales ($f \gtrsim 3$ Hz).

For the observed electromagnetic waves with $f \gtrsim f_{\text{cp}}$, one basic problem is the mode nature. Since SFR streams against the magnetic field (Figure 1), the observed left-hand

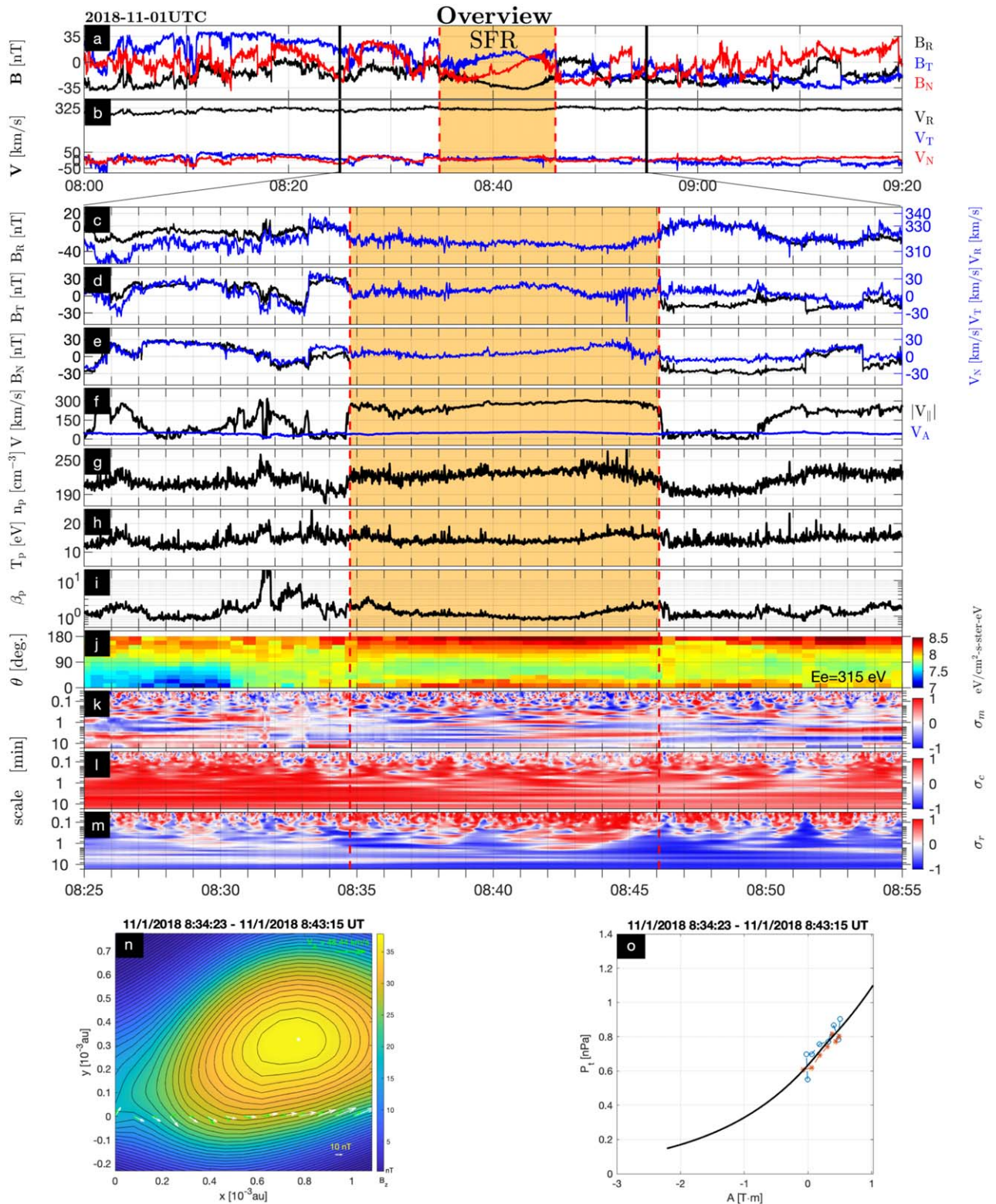


Figure 1. Overview of the SFR event, which arises during 08:34:45 UT–08:46:05 UT (the region between two vertical dashed lines). (a) Magnetic field and (b) solar wind velocity in RTN coordinates from 08:00:00 UT to 09:20:00 UT on 2018 November 1. (c)–(n) Zoom in on the time interval of 08:25:00 UT–08:55:00 UT: (c) B_R and V_R ; (d) B_T and V_T ; (e) B_N and V_N ; (f) the magnitude of the solar wind velocity $|V_{\parallel}|$ along the magnetic field and the Alfvén speed V_A ; (g) proton number density n_p ; (h) proton temperature T_p ; (i) the ratio of proton thermal to magnetic pressure, β_p ; (j) electron pitch angle distribution at $E_e = 315$ eV; (k) normalized magnetic helicity σ_m ; (l) normalized cross helicity σ_c ; and (m) normalized residual energy σ_r . (n)–(o) Grad–Shafranov reconstruction for the flux rope z -axis = $[-0.383, 0.321, -0.866]$ in RTN coordinates. (n) The standard cross-section map, where the colored background represents the axial magnetic field B_z (the maximum B_z corresponds to the white dot), and the black curves denote the transverse magnetic field B_t . The white and green arrows mark the B_t and V_t along the spacecraft path $y = 0$. (o) P_t vs. A , where the blue circles and red stars represent the first and second halves of $P_t(A)$, respectively.

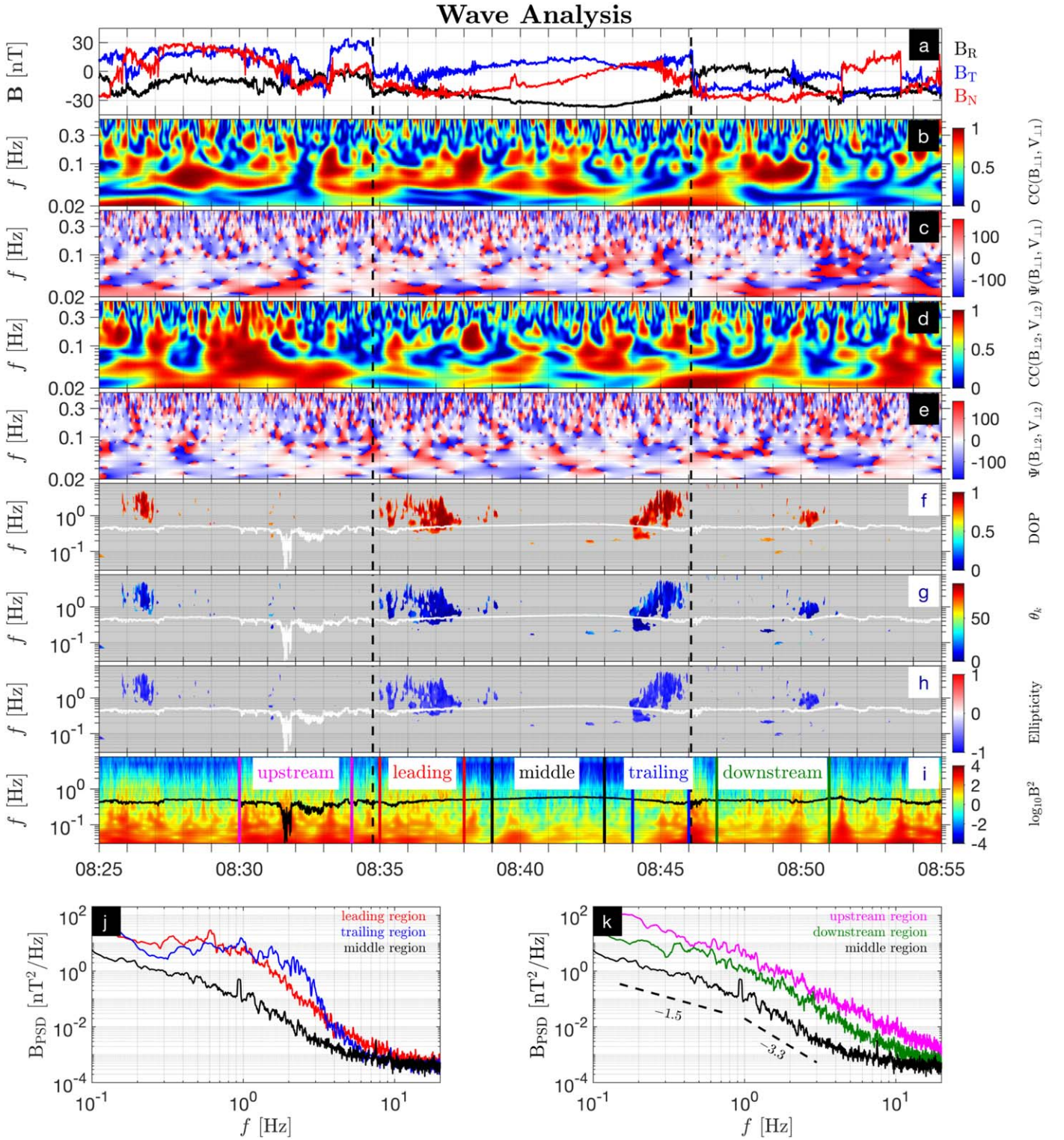


Figure 2. Wave analysis. (a) Magnetic field in RTN coordinates. (b)–(e) Correlation analysis between perpendicular magnetic field B_{\perp} and velocity V_{\perp} fluctuations in 0.02–0.57 Hz: (b) and (d) show the coherence coefficient $CC(B_{\perp}, V_{\perp})$, and (c) and (e) show the coherence phase angle $\Psi(B_{\perp}, V_{\perp})$. (f)–(i) Polarization analysis for magnetic field data: (f) degree of polarization (DOP), (g) wave normal angle θ_k , (h) ellipticity ϵ , and (i) the power spectral density of the magnetic field B_{PSD} . (j)–(k) B_{PSD} in different regions: upstream region during 08:30:00 UT–08:34:00 UT, leading region during 08:35:00 UT–08:38:00 UT, middle region during 08:39:00 UT–08:43:00 UT, trailing region during 08:44:00 UT–08:46:00 UT, and downstream region during 08:47:00 UT–08:51:00 UT.

electromagnetic waves can be either a backward Alfvén/ion-cyclotron (A/IC) mode wave or a forward fast-magnetosonic/whistler (FM/W) mode wave in the plasma frame (Zhao et al. 2020). Unfortunately, the plasma measurements from PSP do not include the high-resolution data, and consequently we

cannot identify the wave mode by using the correlation between the velocity and magnetic field fluctuations (Zhao et al. 2020). Recently, Mozer et al. (2020) explore the distribution of the electric field effective antenna length L_{eff} as a function of the wave frequency with PSP measurements,

and they identify the wave mode by comparing L_{eff} with the antenna half-geometric length. Here we follow their method to identify the wave mode. Since the measured differential potentials dV are restricted to $(x-y)$ plane in the spacecraft frame, we will estimate L_{eff} in the spacecraft frame.

At first, we use the minimum variance analysis (MVA; e.g., Sonnerup & Cahill 1967) to find out the direction of the wavevector \mathbf{k} . Since MVA can result in the 180° ambiguity of $\mathbf{k}/|\mathbf{k}|$, we use the z -direction Poynting flux S_z to yield the uncertainty of $\mathbf{k}/|\mathbf{k}|$ through $S_z \cdot \mathbf{k}/|\mathbf{k}| > 0$. Figure 3(a) presents MVA results in the SFR leading region, where the smoothing timescale is 4 s. The ratio of intermediate to minimum eigenvalues $\lambda_{\text{int}}/\lambda_{\text{min}}$ is larger than 10 in most time intervals, indicating that MVA is valid therein. The ratio of maximum to intermediate eigenvalue $\lambda_{\text{max}}/\lambda_{\text{int}}$ approximates 1 in $\lambda_{\text{int}}/\lambda_{\text{min}} \gtrsim 10$ regions, indicating that the waves are circularly polarized (also see Figure 2). The observed waves have the wave normal angle $\theta \simeq 176^\circ$, which means that these waves are nearly antiparallel propagation with respect with the background magnetic field.

Second, using the wavevector direction and observed parameters, we can directly give the dispersion relations and linear responses among all wave variables. We recently developed a wave theory in the spacecraft frame based on the cold two-fluid model, where the plasma bulk flow and the wavevector can be in arbitrary direction (J. Zhao 2020, in preparation). Under the averaged wave and plasma parameters during the time interval of 08:36:50 UT–08:37:10 UT (labeled by two dotted lines in Figure 3(a)), i.e., $\mathbf{k}/|\mathbf{k}| = [0.074, -0.73, -0.68]$, $n_p = n_e = 219 \text{ cm}^{-3}$, $\mathbf{V} = [-63, 6, -356] \text{ km s}^{-1}$, and $\mathbf{B} = [-0.8, 23, 22] \text{ nT}$, the corresponding low-frequency electromagnetic wave modes are shown in Figure 3(b). There are two modes behaving the left-hand polarization ($\arg(B_y/B_x) = -90^\circ$), i.e., the A/IC mode wave with $V_{\perp 1}/B_{\perp 1} > 1$ (backward propagation in the plasma frame; labeled by dashed lines), and the FM/W mode wave with $0 > V_{\perp 1}/B_{\perp 1} > -1$ (forward propagation in the plasma frame; labeled by dotted lines). The candidates of the observed waves (0.3–3 Hz; see Figure 2) correspond to the A/IC mode wave with $\lambda_p|k| \simeq 0.1 - 1.1$, $E_x/V_A B_y \simeq -8.9$ to -8.3 , and $E_y/V_A B_x \simeq 8.0 - 8.2$ (thick dashed lines), and the FM/W mode wave with $\lambda_p|k| \simeq 0.2 - 4.7$, $E_x/V_A B_y \simeq -5.9$ to -0.5 , and $E_y/V_A B_x \simeq 4.2 - 6.8$ (thick dotted lines). It should be emphasized that the FM/W mode wave cannot explain the observed high-frequency waves with $f \sim 3 \text{ Hz}$.

Lastly, using the theoretical electromagnetic ratios and the observed electromagnetic fields, we can estimate the electric field effective antenna length through $L_{\text{eff}} = (dV/V_A \mathbf{B})^{\text{obs}} / (E/V_A \mathbf{B})^{\text{theory}}$. The observed $(dV/V_A \mathbf{B})$ is shown in Figure 3(c), which also exhibits the power spectral densities of $dV = E L_{\text{eff}}$ and \mathbf{B} . Both the observed $dV_x/V_A B_y$ and $dV_y/V_A B_x$ are about 10 in the frequency range of 0.3–3 Hz. The theoretical predictions of L_{eff} are presented in Figure 3(d). For the A/IC mode wave, $\bar{L}_{\text{eff}}(E_x/V_A B_y)$ and $\bar{L}_{\text{eff}}(E_y/V_A B_x)$ are about 2.6 m and 1.2 m, respectively, where \bar{L}_{eff} is the mean electric field effective antenna length. The FM/W mode wave predicts longer L_{eff} than that estimated by the A/IC mode wave, even much longer than the antenna half-geometric length of 3.5 m (see L_{eff} for the FM/W mode wave with $\lambda_p|k| \sim 2.5 - 4.5$).

Similarly, Figure 4 gives the L_{eff} distributions in the SFR trailing region. For the A/IC mode wave, $\bar{L}_{\text{eff}}(E_x/V_A B_y)$ and $\bar{L}_{\text{eff}}(E_y/V_A B_x)$ are about 1.4 m and 1.5 m, respectively. For the FM/W mode wave with $\lambda_p|k| \simeq 0.1 - 1.4$, $\bar{L}_{\text{eff}}(E_x/V_A B_y) \simeq 1.7 \text{ m}$ and $\bar{L}_{\text{eff}}(E_y/V_A B_x) \simeq 1.9 \text{ m}$. For the short-scale FM/W mode

wave ($\lambda_p|k| \simeq 7.7 - 9.0$), \bar{L}_{eff} is much larger than 3.5 m, and it is unreasonable.

Combining the results of the wave dispersion and L_{eff} in Figures 3 and 4, we conclude that the A/IC mode wave gives L_{eff} closer to the values given by Mozer et al. (2020), i.e., $L_{\text{eff}} = 1.15 \text{ m}$ at 1 Hz and 0.98 m at 3 Hz, and the FM/W mode wave cannot explain the high-frequency branch of the observed waves in the SFR leading region. Therefore, we propose that the observed waves with $f \gtrsim f_{\text{cp}}$ are A/IC mode waves.

Figure 5 further gives the wave frequency f_{plas} and wavelength λ of the observed $f \gtrsim f_{\text{cp}}$ waves in the plasma frame. Since the observed waves are nearly antiparallel to the background magnetic field, we calculate f_{plas} and λ using the analytical dispersion relations of parallel and antiparallel A/IC and FM/W mode waves in the spacecraft frame (Zhao et al. 2020). Using the dispersion relations of the A/IC mode wave,

$$2\pi f_{\text{sc}} = V_{\parallel} k - V_A k (\lambda_p k / 2 + \sqrt{1 + \lambda_e^2 k^2 + \lambda_p^2 k^2 / 4}) / (1 + \lambda_e^2 k^2), \quad (1)$$

and the FM/W mode wave,

$$2\pi f_{\text{sc}} = V_{\parallel} k - V_A k (\lambda_p k / 2 - \sqrt{1 + \lambda_e^2 k^2 + \lambda_p^2 k^2 / 4}) / (1 + \lambda_e^2 k^2), \quad (2)$$

we can obtain both $\lambda = 2\pi/|k|$ and $f_{\text{plas}} = |f_{\text{sc}} - V_{\parallel} k / 2\pi|$. Here we only consider minimum and maximum f_{sc} of the observed quasi-monochromatic waves at each time. Figure 5(a) shows $f_{\text{plas}} \sim 0.03 - 0.3 \text{ Hz}$ and $\lambda \sim 60 - 1000 \text{ km}$ for A/IC mode waves in the SFR leading region, where the proton inertial length λ_p and the proton gyroradius ρ_p are about 15 km and 19 km, respectively. Figure 5(b) shows $f_{\text{plas}} \sim 0.02 - 0.3 \text{ Hz}$ and $\lambda \sim 60 - 2000 \text{ km}$ for A/IC mode waves in the SFR trailing region, where $\lambda_p \simeq 15 \text{ km}$ and $\rho_p \simeq 20 \text{ km}$. Since f_{plas} is close to f_{cp} , the observed waves are indeed ion-cyclotron waves. Besides, as the frequency of the FM/W mode wave is cutoff at $\sim 2 \text{ Hz}$ in the SFR leading region (see Figure 3), there exist gaps in the f_{plas} and λ distributions relating to FM/W mode waves therein.

4. Discussion and Summary

Using PSP measurement at 0.23 au, this paper reports an interesting SFR event in the slow solar wind, which contains both Alfvénic waves and ion-cyclotron waves. This SFR event is surrounded by Alfvénic waves and Alfvénic structures. Alfvénic waves inside and outside of this SFR have frequencies below $\sim 0.3 \text{ Hz}$, and are mainly propagating outward from the Sun. Moreover, the turbulence composed by these Alfvénic waves cascades to sub-ion scales (corresponding to $f \gtrsim 3 \text{ Hz}$), and the spectral index changes from -1.5 ($f \lesssim 1 \text{ Hz}$) to -3.3 ($f \gtrsim 1 \text{ Hz}$). For the source of the observed Alfvénic waves and Alfvénic turbulence, referring to the suggestion given by Gosling et al. (2010), they may exist within the flux rope if this SFR originates from a small-scale coronal mass ejection. However, if this SFR results from the MHD turbulence in the solar wind (Zank et al. 2017), it would be a natural result that SFRs contain the waves and turbulence coming from the surrounding environment. Besides, Alfvénic waves can be produced due to the change of the magnetic field topology through magnetic reconnections, and the nonlinear interaction

Identifying Wave Mode in Leading Region

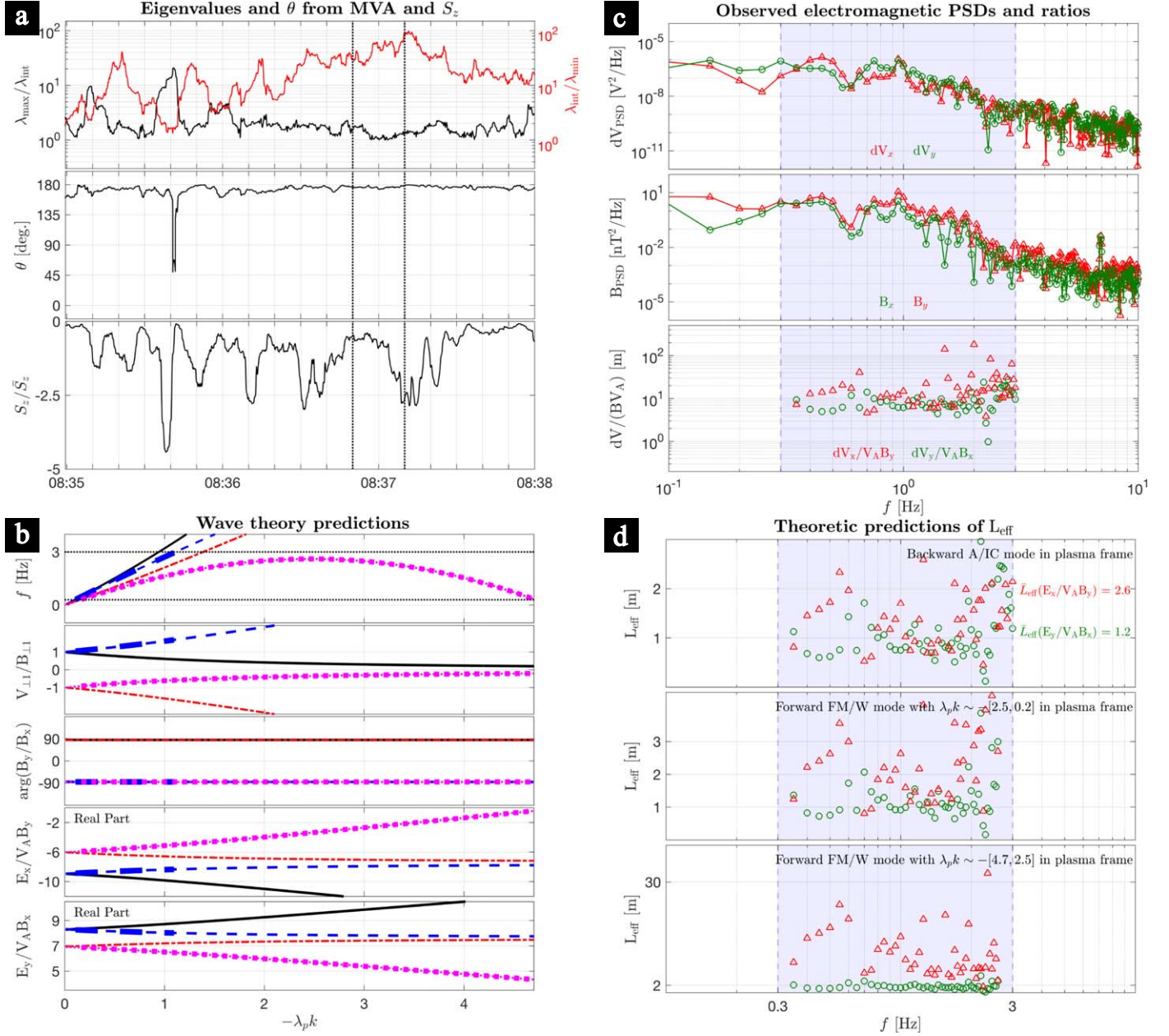


Figure 3. Identifying wave mode in the SFR leading region. (a) MVA analysis results: from top to bottom, ratios among three eigenvalues (λ_{max} , λ_{int} , and λ_{min}), normal angle θ , normalized z -direction Poynting flux S_z/\bar{S}_z , where \bar{S}_z is the mean S_z . (b) Wave theory predictions in the spacecraft frame: from top to bottom, dispersion relation, ratio of the velocity to magnetic field fluctuations perpendicular to the magnetic field, argument of B_y/B_x , real part of $E_x/V_A B_y$, and real part of $E_y/V_A B_x$, where the solid, dashed, dotted-dashed, and dotted lines denote forward FM/W mode, forward A/IC mode, backward FM/W mode, and backward A/IC mode waves, respectively. (c) Electromagnetic PSDs and ratios between electric and magnetic field fluctuations: from top to bottom, PSDs of the measurement differential potential dV , PSDs of the magnetic field B , and $dV/V_A B$. (d) Theoretic predictions of L_{eff} : from top to bottom, the values resulting from backward A/IC mode waves, forward FM/W mode waves with $\lambda_p k \sim -[2.5, 0.2]$, and forward FM/W mode waves with $\lambda_p k \sim -[4.7, 2.5]$ in the plasma frame, respectively, where the triangle and circular symbols represent $L_{\text{eff}}(E_x/V_A B_y)$ and $L_{\text{eff}}(E_y/V_A B_x)$, respectively.

among Alfvénic waves could further produce the Alfvénic turbulence (e.g., Cranmer et al. 2007). These three possible sources cannot be distinguished via single spacecraft observation. It should be noted that Alfvénic waves and Alfvénic turbulence also exist in magnetic clouds (e.g., Li et al. 2017; Guo et al. 2019).

We also identify quasi-monochromatic and left-hand polarized electromagnetic waves with $f \gtrsim f_{\text{cp}}$ at SFR leading and trailing edges. As the outward A/IC and inward FM/W mode waves in the plasma frame are two candidates to explain these

high-frequency electromagnetic waves, to distinguish these two modes, we investigate the wave dispersion relation and estimate the electric field effective length based on the wave theory in the spacecraft frame. We find that FM/W mode waves cannot explain the observed waves with $\sim 2\text{--}3$ Hz at the SFR leading edge. Moreover, the electric field effective length corresponding to the FM/W mode wave is larger than that estimated from the A/IC mode wave, and the latter seems to be closer to the values given by Mozer et al. (2020). Therefore, we conclude that the observed $f \gtrsim f_{\text{cp}}$ electromagnetic waves

Identifying Wave Mode in Trailing Region

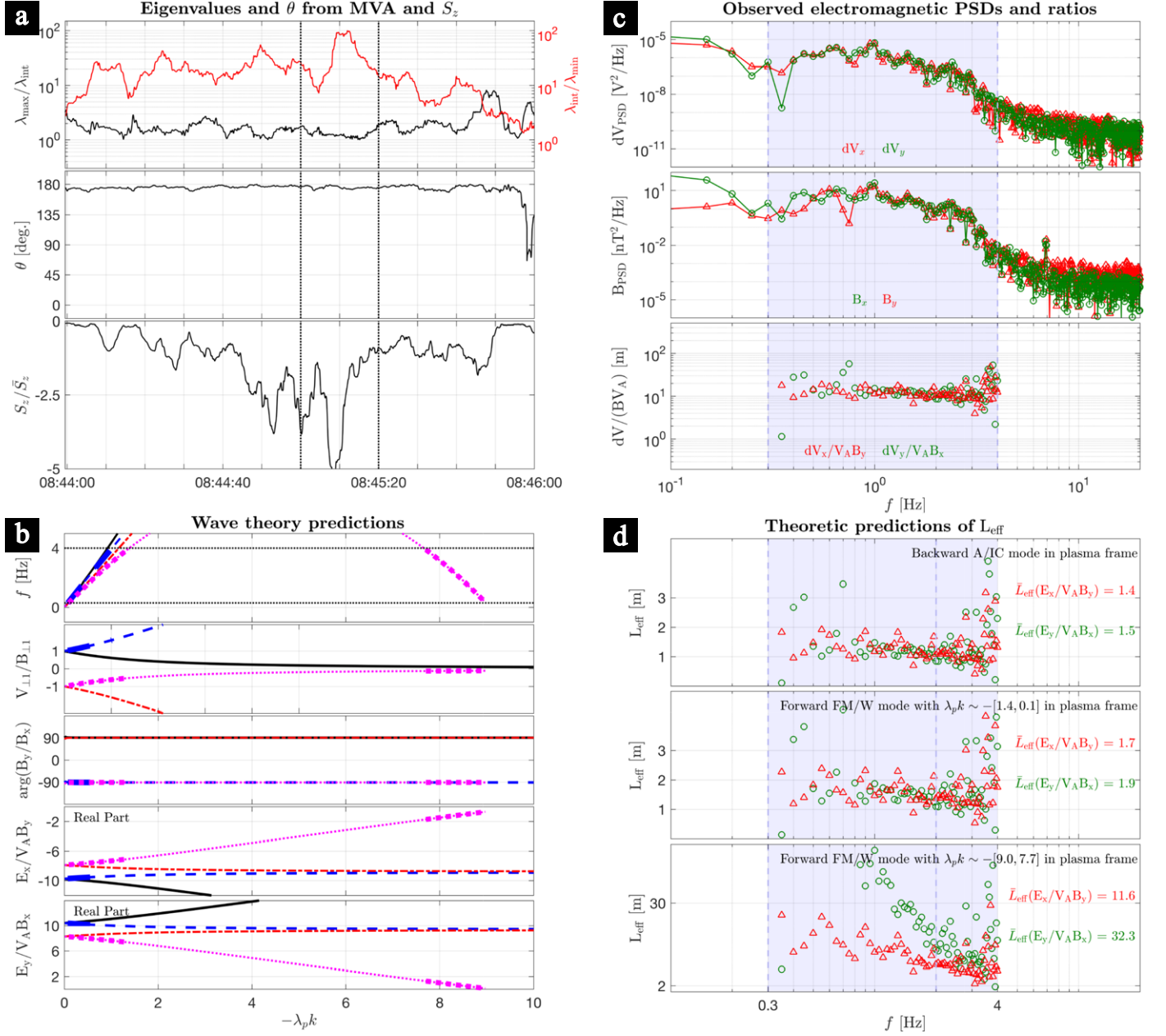


Figure 4. Same as in Figure 3. Identifying the wave mode in the SFR trailing region.

correspond to A/IC mode waves. In addition, PSP also detects ion-cyclotron waves in steady solar wind (Bowen et al. 2020; Verniero et al. 2020), and this study gives direct observational evidences of ion-cyclotron waves in SFR.

The observed ion-cyclotron waves can be driven by the ion perpendicular temperature anisotropy instability or the ion beam instability (e.g., Gary 1993; Liu et al. 2019; Sun et al. 2019). Since the SFR flow velocity is nearly the same as the speed of ambient solar wind, SFR cannot significantly compress the ambient plasma, inducing large ion perpendicular temperature anisotropy therein. On the other hand, the proton beam can produce both A/IC and FM/W mode waves along the beam direction (e.g., Liu et al. 2019), which is inconsistent with the presence of only one wave mode, i.e., outward A/IC mode waves. As a consequence, we propose that the observed

waves may not be locally produced by the ion perpendicular temperature anisotropy instability or the ion beam instability.

Besides, SFRs with medium and high Alfvénicity are normally discarded in automated identification procedures, which use a low Walén slope threshold (≤ 0.3) or low normalized cross helicity (≤ 0.3) (e.g., Chen et al. 2020; Zhao et al. 2020a, 2020b). The Walén slope in our event is about 0.37 during 08:34:45 UT–08:46:05 UT in a de Hoffman–Teller (HT) frame where the HT speed is $[332.34, 5.83, 12.99] \text{ km s}^{-1}$, and this event is not listed in the database given by Chen et al. (2020) and Zhao et al. (2020a, 2020b). It should be noted that Gosling et al. (2010) have examined the SFR database recognized by several identification procedures (e.g., Moldwin et al. 1995, 2000; Feng et al. 2007; Cartwright & Moldwin 2008), and they concluded that SFRs with high Alfvénicity are relatively rare in solar wind. Actually, the

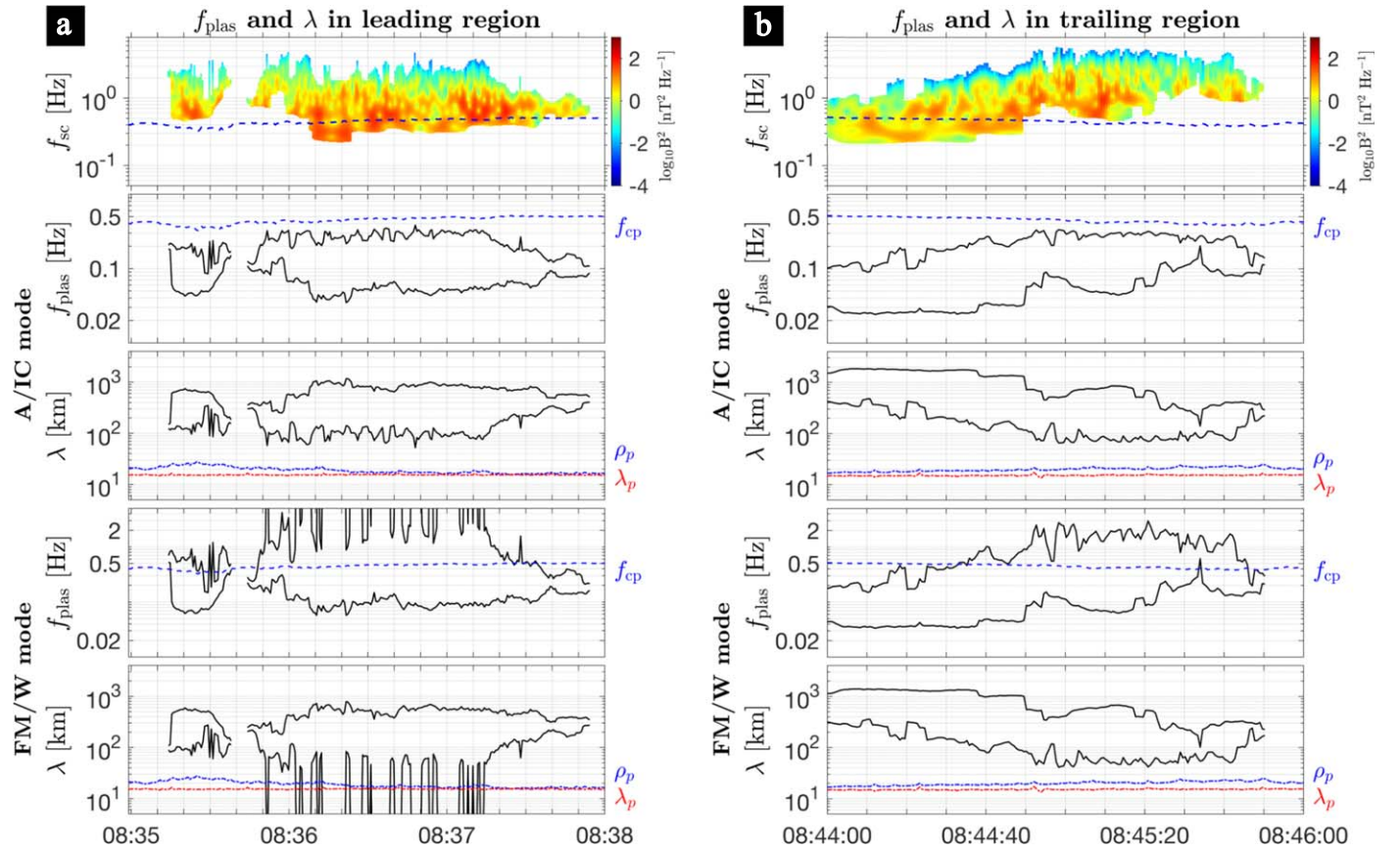


Figure 5. The wave frequency f_{plas} and wavelength λ in the plasma frame: (a) the SFR leading region and (b) the SFR trailing region. From top to bottom, the frequency range of quasi-monochromatic electromagnetic waves labeled by B_{PSD} , f_{plas} of A/IC mode waves, λ of A/IC mode waves, f_{plas} of FM/W mode waves, and λ of FM/W mode waves. The blue dashed lines represent the proton cyclotron frequency f_{cp} ; and the blue and red dashed-dotted lines denote the proton gyroradius ρ_p and the proton inertial length λ_p , respectively.

SFR event database analyzed by Gosling et al. (2010) suffer a low Walén slope limit. There may be still no robust conclusion on the occurrence rate of SFR with medium and high Alfvénicity. Moreover, Hu et al. (2018) found that the duration of SFRs (from 10 minutes to several 100 minutes) follows a power-law distribution. Most events detected by PSP have durations of the order of 10 minutes (also see Chen et al. 2020; Zhao et al. 2020a, 2020b). Alfvénic structures can also arise at a timescale of 10 minutes (e.g., Bale et al. 2019; Kasper et al. 2019). Therefore, an effective identification method needs to be developed in order to discriminate SFRs with medium and high Alfvénicity from Alfvénic structures, which will be studied in the future.

This work was supported by the NNSFC 41974203, 41531071, and 11673069. We acknowledge the NASA Parker Solar Probe Mission and the SWEAP team led by J. Kasper and the FIELDS team led by S. D. Bale for use of data. The data can be downloaded from the NASA CDAWeb (<https://cdaweb.gsfc.nasa.gov/pub/data/psp/>). The SWEAP and FIELDS experiments on the Parker Solar Probe spacecraft were designed and developed under NASA contract NNN06AA01C.

ORCID iDs

Chen Shi <https://orcid.org/0000-0002-9166-1036>
 Jinsong Zhao <https://orcid.org/0000-0002-3859-6394>
 Jia Huang <https://orcid.org/0000-0002-9954-4707>
 Teyan Wang <https://orcid.org/0000-0003-3072-6139>
 Dejin Wu <https://orcid.org/0000-0003-2418-5508>

Yu Chen <https://orcid.org/0000-0002-0065-7622>
 Qiang Hu <https://orcid.org/0000-0002-7570-2301>
 Justin C. Kasper <https://orcid.org/0000-0002-7077-930X>
 Stuart D. Bale <https://orcid.org/0000-0002-1989-3596>

References

- Bale, S. D., Badman, S. T., Bonnell, J. W., et al. 2019, *Natur*, 576, 237
 Bale, S. D., Goetz, K., Harvey, P. R., et al. 2016, *SSRv*, 204, 49
 Bowen, T. A., Mallet, A., Huang, J., et al. 2020, *ApJS*, 246, 66
 Cartwright, M. L., & Moldwin, M. B. 2008, *JGRA*, 113, A09105
 Cartwright, M. L., & Moldwin, M. B. 2010, *JGRA*, 115, A08102
 Chen, Y., & Hu, Q. 2020, *ApJ*, 894, 25
 Chen, Y., Hu, Q., & le Roux, J. A. 2019, *ApJ*, 881, 58
 Chen, Y., Hu, Q., Zhao, L., et al. 2020, *ApJ*, 903, 76
 Cramer, S. R., van Ballegoijen, A. A., & Edgar, R. J. 2007, *ApJS*, 171, 520
 Feng, H. Q., Wu, D. J., & Chao, J. K. 2007, *JGRA*, 112, A02102
 Feng, H. Q., Wu, D. J., Lin, C. C., et al. 2008, *JGRA*, 113, A12105
 Fox, N. J., Velli, M. C., Bale, S. D., et al. 2016, *SSRv*, 204, 7
 Gary, S. P. 1993, *Theory of Space Plasma Microinstabilities* (Cambridge: Cambridge Univ. Press)
 Gosling, J. T., Teh, W.-L., & Eriksson, S. 2010, *ApJL*, 719, L36
 Grinstead, A., Moore, J. C., & Jevrejeva, S. 2004, *NPGeo*, 11, 561
 Guo, J., Wang, Z., Feng, X., et al. 2019, *ApJL*, 874, L19
 Hau, L.-N., & Sonnerup, B. U. Ö 1999, *JGR*, 104, 6899
 Hu, Q., & Sonnerup, B. U. Ö 2001, *GeoRL*, 28, 467
 Hu, Q., & Sonnerup, B. U. Ö 2002, *JGRA*, 107, 1142
 Hu, Q., Zheng, J., Chen, Y., et al. 2018, *ApJS*, 239, 12
 Huang, J., Liu, Y. C.-M., Peng, J., et al. 2017, *JGR*, 122, 6927
 Huang, J., Liu, Y. C.-M., Peng, J., et al. 2018, *JGR*, 123, 7167
 Kasper, J. C., Abiad, R., Austin, G., et al. 2016, *SSRv*, 204, 131
 Kasper, J. C., Bale, S. D., Belcher, J. W., et al. 2019, *Natur*, 576, 228
 Kilpua, E., Koskinen, H. E. J., & Pulkkinen, T. I. 2017, *LRS*, 14, 5

- Klein, L. W., & Burlaga, L. F. 1982, *JGR*, **87**, 613
- Li, H., Wang, C., Richardson, J. D., et al. 2017, *ApJL*, **851**, L2
- Liu, Y. D., Luhmann, J. G., Kajdič, P., et al. 2014, *NatCo*, **5**, 3481
- Liu, Z., Zhao, J., Sun, H., et al. 2019, *ApJ*, **874**, 128
- Moldwin, M. B., Ford, S., Lepping, R., et al. 2000, *GeoRL*, **27**, 57
- Moldwin, M. B., Phillips, J. L., Gosling, J. T., et al. 1995, *JGR*, **100**, 19903
- Mozer, F. S., Agapitov, O. V., Bale, S. D., et al. 2020, *JGRA*, **125**, e2020JA027980
- Nieves-Chinchilla, T., Szabo, A., Korreck, K. E., et al. 2020, *ApJS*, **246**, 63
- SantofíK, O., Parrot, M., & Lefeuvre, F. 2003, *RaSc*, **38**, 1010
- Shen, C., Chi, Y., Wang, Y., Xu, M., & Wang, S. 2017, *JGRA*, **122**, 5931
- Shen, C., Wang, Y., Pan, Z., et al. 2014, *JGRA*, **119**, 5107
- Sonnerup, B. U. O., & Cahill, L. J. 1967, *JGR*, **72**, 171
- Sun, H., Zhao, J., Xie, H., et al. 2019, *ApJ*, **884**, 44
- Telloni, D., Perri, S., Bruno, R., et al. 2013, *ApJ*, **776**, 3
- Tian, H., Yao, S., Zong, Q., et al. 2010, *ApJ*, **720**, 454
- Verniero, J. L., Larson, D. E., Livi, R., et al. 2020, *ApJS*, **248**, 5
- Yu, W., Farrugia, C. J., Galvin, A. B., et al. 2016, *JGRA*, **121**, 5005
- Yu, W., Farrugia, C. J., Lugaz, N., et al. 2014, *JGRA*, **119**, 689
- Zank, G. P., Adhikari, L., Hunana, P., et al. 2017, *ApJ*, **835**, 147
- Zhao, J., Wang, T., Graham, D. B., et al. 2020, *ApJ*, **890**, 17
- Zhao, L.-L., Zank, G. P., Adhikari, L., et al. 2020a, *ApJS*, **246**, 26
- Zhao, L.-L., Zank, G. P., Hu, Q., et al. 2020b, arXiv:2010.04664
- Zheng, J., & Hu, Q. 2018, *ApJL*, **852**, L23